Scientific Reports

https://doi.org/10.1038/s41598-026-41667-0

Article in Press

Dual-band graphene-assisted metamaterial absorber with machine learning integration for high-sensitivity THz biosensing

Received: 7 November 2025

Accepted: 23 February 2026

Published online: 10 March 2026

Cite this article as: Gupta S., Gosi V.C., Pareek P. *et al.* Dual-band graphene-assisted metamaterial absorber with machine learning integration for high-sensitivity THz biosensing. *Sci Rep* (2026). https://doi.org/10.1038/s41598-026-41667-0

Shagun Gupta, Vaishnavi Chandrashekar Gosi, Parth Pareek & Patri Upender

Dual-Band Graphene-Assisted Metamaterial Absorber with Machine Learning Integration for High-Sensitivity THz Biosensing

Shagun Gupta[1], Vaishnavi Chandrashekar Gosi[2], Parth Pareek[3], Patri Upender*[4]

[1, 2, 3, *4]School of Electronics Engineering, Vellore Institute of Technology, Chennai, Tamil Nadu, 600127, India.

(*Corresponding Author Email Address: upender.p@vit.ac.in)

Abstract-

In this work, a compact dual-band terahertz (THz) metamaterial absorber integrated with graphene is presented for high-performance biosensing applications. The structure is composed of four concentric octagonal rings, where two are metallic and two are graphene-based, supported on a SiO_2 substrate backed by a gold ground plane. The dual-resonant response is achieved through the metallic rings, while the graphene layers enhance absorption and tunability by improving impedance matching with free space. The absorber demonstrates near-unity absorption at 0.9623 THz and 1.4079 THz, with maximum sensitivities of 1.7435 THz/RIU and 1.475 THz/RIU, and corresponding high figures of merit and quality factors, making it highly suitable for precise biosensing. A detailed parametric analysis confirms the influence of structural dimensions on absorption efficiency, while the equivalent circuit model validates the underlying resonance mechanisms. Furthermore, machine learning models are employed to predict absorption characteristics and support biosensing tasks such as virus detection, thereby reducing the need for repeated full-wave simulations. The proposed design effectively combines compact geometry, high sensitivity, excellent selectivity, and ML-assisted optimization, positioning it as a versatile candidate for next-generation THz biosensing and biomedical diagnostics.

Keywords: Metamaterial, Absorber, Sensitivity, Machine Learning, Biosensor.

I. Introduction

The terahertz (THz) frequency range, spanning approximately 0.1–10 THz, has attracted significant attention due to its unique potential in fields such as medical diagnostics, security screening, high-speed communications, and non-destructive testing [1], [2], [3]. Devices operating in this spectrum can exploit the ability of THz waves to penetrate non-conductive materials while also being sensitive to molecular vibrations and rotational transitions. Despite these advantages, practical THz systems face challenges such as the lack of compact, efficient components for the generation, detection, and manipulation of THz radiation [4], [5], [6], [7]. Among the emerging solutions, absorbers play a crucial role by suppressing unwanted reflections and enhancing device performance in sensing, imaging, and stealth applications. Conventional absorbers, however, are often limited by their thickness, narrowband response, and lack of tunability. To overcome these drawbacks, metamaterial-based absorbers have been introduced, leveraging artificially engineered subwavelength unit cells to achieve tailored electromagnetic responses not found in natural materials. Metamaterials provide precise control over effective permittivity and permeability, enabling perfect absorption at designed frequencies through impedance matching with free space [8], [9], [10], [11]. By carefully designing resonant structures, these absorbers can be made compact, lightweight, and capable of achieving multi-band or broadband operation. Furthermore, the integration of tunable materials such as graphene into metamaterial designs introduces dynamic control over resonance frequency and absorption strength, making them highly suitable for next-generation THz applications, including biosensing, communication, and reconfigurable photonic systems [12], [13], [14], [15].

Several researchers have investigated advanced materials to enhance the tunability of metamaterial absorbers. Graphene has been widely employed due to its electrically controllable surface conductivity, enabling dynamic adjustment of absorption characteristics across the terahertz band. Vanadium dioxide (VO_2) has also been explored, as it exhibits a temperature-driven insulator-to-metal phase transition that allows switching between transparent and conductive states, making it suitable for reconfigurable absorber designs [16], [17], [18], [19]. More recently, MXenes, a family of two-dimensional transition metal carbides and nitrides, have attracted attention because of their excellent electrical conductivity, chemical stability, and wide tunability through surface functionalization [8], [20], [21]. These materials provide versatile platforms for designing adaptive absorbers, where the resonance behaviour can be tailored in real time for applications such as sensing, switching, and communication. Building on these material innovations, such as graphene, vanadium dioxide, and MXenes that offer tunability and adaptability, researchers have also focused on tailoring absorber designs to achieve desired operational characteristics [22], [23], [24]. While single-band absorbers provide efficient performance at one resonance, they fall short in multifunctional scenarios. This has led to growing interest in dual-band absorbers, which, by supporting two distinct resonances, extend the operational flexibility of devices and enable broader applications in THz sensing, imaging, and communications [24], [25], [26], [27].

Some of the researchers have developed dual-band absorbers [28], [29], [30], [31], [32], [33], [34], [35], [36], [37]. In recent years, several researchers have focused on the development of dual-band terahertz metamaterial absorbers for biosensing applications, aiming to enhance sensitivity and diagnostic accuracy. For example, the work reported in [28] introduced a dual-band metamaterial sensor based on a gold octagonal loop, designed specifically for cancer detection. The device achieved perfect absorption at resonance frequencies near 1.994 THz and 2.7 THz, with absorption levels of 100% and 88%, respectively. Notably, the sensor exhibited remarkable refractive index sensitivities of 600 GHz/RIU and 800 GHz/RIU, along with quality factors of 12.24 and 8.9. This performance enabled reliable detection of various cancer cell types, such as breast, cervical, and MCF-7, demonstrating its strong biomedical relevance. Similarly, a tunable stereo metamaterial biosensor was reported in [29], where a double-layer configuration combining electric and magnetic resonances enabled independently adjustable dual resonances across the 0.5–1.8 THz range. This design not only addressed the limitations of single-frequency sensors but also achieved a maximum sensitivity of 930.4 GHz/RIU with a high Q factor of 23.7 and a FOM of 12.53. The ability to fine-tune resonant modes significantly enhances its adaptability for detecting biomolecules with varying spectral responses, making it a versatile platform for practical terahertz biosensing. Furthermore, the study in [30] demonstrated an extremely compact dual-band biosensor optimised for non-melanoma skin cancer diagnostics. The proposed metamaterial absorber achieved near-perfect absorption (>99.5%) at 0.78 THz and 0.904 THz, supported by sensitivities of 0.0515 and 0.076 THz/RIU, quality factors of 12.5 and 13.5, and FOM values of 0.86 and 1.16. Owing to the strong interaction of THz waves with polar biomolecules, this compact absorber shows promise for early and accurate identification of basal cell carcinomas. Building upon these advancements, subsequent works have further diversified the designs of dual-band metamaterial absorbers and sensors across different frequency regimes. For instance, the study in [31] introduced a split metal stacking ring resonator (SMSRR)–based terahertz sensor, which achieved dual resonances at 0.97 THz and 2.88 THz. The design demonstrated multi-point frequency matching with analytes, thereby improving sensing reliability. Sensitivities of 304 GHz/RIU and 912 GHz/RIU were reported, highlighting the effectiveness of such structures in enhancing the detection of low-concentration biomolecules.

In [32], a compact dual-band absorber was presented, relying on LC resonance and dipolar responses to achieve near-unity absorption at 7.51 THz and 8.08 THz. Unlike more complex metamaterial geometries, this design emphasised ease of fabrication while maintaining strong performance. However, the polarisation sensitivity of the structure was noted, which may limit its universality in practical applications. Graphene-based tunable absorbers have also gained attention, as demonstrated in [33]. Here, a dual-band absorber operating at 5.1 THz and 11.7 THz was designed with chemical potential–dependent tunability. By leveraging graphene plasmon resonances, the structure achieved sharp and narrow absorption peaks with near-perfect absorption, even under oblique incidence up to 8°. The reported sensitivity of 4.72 THz/RIU, along with high FOM and Q values (14 and 32.49), underlines the potential of graphene integration for adaptive biosensing platforms.

While most designs target terahertz frequencies, efforts have also extended to the visible spectrum. The work in [34] proposed a dual-frequency absorber inspired by the geometry of ancient Chinese coins, integrating Au/SiO2/Au layers. This structure achieved near-perfect absorption (99.9%) at two distinct visible wavelengths and demonstrated tunability through geometric parameter adjustments, opening possibilities for photonic and optoelectronic device integration. Additionally, in [35], a dual-band metamaterial absorber was developed for electromagnetic interference (EMI) shielding in communication systems, particularly GSM (1.8 GHz) and sub-6 GHz 5G (3.5 GHz). The design achieved absorption peaks of 98.7% and 99.7% with excellent angular stability up to 60°. Equivalent circuit modelling confirmed the absorption mechanisms, and the fabricated prototype exhibited strong agreement with simulations. Importantly, the absorber demonstrated high shielding effectiveness of 40.12 dB and 36.81 dB at the respective bands, underscoring its suitability for practical EMI control in modern wireless technologies.

Even though the above-mentioned designs have demonstrated promising absorption characteristics and valuable application potential, they still present certain limitations that restrict their overall efficiency in practical scenarios. Many of the reported structures suffer from relatively low sensitivity, which reduces their ability to precisely detect minute variations in the analyte refractive index. In addition, several of these designs rely on complex geometries or multi-layered configurations, which not only increase fabrication challenges but also make the structures less compact. Another drawback lies in the limited quality factor observed in some absorbers, where broader resonance peaks reduce spectral selectivity and thereby compromise sensing accuracy. Furthermore, polarization dependence and angular instability in certain designs restrict their adaptability to real-world environments where incident waves may not always be ideally aligned.

These limitations are effectively addressed in the proposed design, which achieves a compact and easily realizable structure without sacrificing performance. By carefully optimizing the resonator configuration and introducing graphene layers for tunability, the design attains significantly enhanced sensitivity, sharper resonances with higher quality factors, and near-unity absorption. The dual-band operation not only broadens functionality but also ensures precise detection across multiple frequency points. Moreover, the simplicity of the structure reduces design complexity while maintaining robustness, thereby overcoming the major shortcomings of earlier works and making it more suitable for advanced terahertz sensing and absorption applications. Additionally, the proposed design goes a step further by integrating machine learning (ML) models, which not only analyze and predict absorption characteristics with high precision but also enable intelligent detection of target biomarkers, including viruses, for biosensing applications. By training ML algorithms on absorption spectra and resonance behavior, the system can rapidly identify subtle variations in the frequency response that are often difficult to distinguish through conventional methods. This integration enhances detection accuracy, reduces analysis time, and supports real-time decision-making, thereby extending the utility of the absorber beyond conventional sensing to advanced biomedical diagnostics.

II. Design Procedure

Fig. 1(a) illustrates the periodic structure of the proposed absorber. The design is based on a unit cell with dimensions of 80 μm × 80 μm, arranged in a periodic array to achieve dual-band absorption characteristics. The incoming terahertz wave interacts with the periodic unit cell, where the carefully engineered multilayer configuration ensures strong confinement and resonance. The bottom gold layer, with a high conductivity of 4.561×10^7 S/m, serves as a perfect reflector, eliminating transmission and ensuring maximum absorption within the designed frequency band. Fig. 1(b) shows the front view of the absorber, where a SiO_2 substrate with permittivity ε = 2.25 and thickness t_{sio2} is placed between the patterned resonator and the ground plane. Graphene tunability is realized through an electrostatic field-effect configuration, as illustrated in the updated Fig. 1(b). A top metal gate is placed above a thin ion-gel or high-κ dielectric layer, forming a capacitor with the graphene sheet. By applying a gate voltage (V_g) of a few volts, the carrier density of graphene can be modulated, enabling variation of its chemical potential (μ_c) from 0.1 eV to 1.0 eV. This modification alters the surface conductivity derived using the Kubo formalism, thereby tuning the absorption response. The lateral positioning of the gate contact and dielectric ensures that the analyte directly interacts with graphene, while remaining electrically isolated from the bias electrodes, making the structure compatible with biosensing applications. The resonator consists of four concentric octagonal rings, strategically designed to support multiple resonance modes. Among these, Rings 1 and 2 are made of gold, while Rings 3 and 4 are composed of graphene. The graphene rings are modeled with an initial chemical potential of 0.1 eV, a temperature of 300 K, and a relaxation time of 1 ps. This hybrid use of gold and graphene provides tunability and strong plasmonic response, enabling efficient dual-band absorption. Fig. 1(c) presents the unit cell view of the absorber, highlighting the arrangement of the four octagonal rings. The varying radii of these rings ensure coupling at different frequencies, thereby producing distinct resonant modes. The geometric symmetry contributes to polarization insensitivity, while the material combination ensures both high-quality resonance and tunability across the terahertz spectrum. Fig. 1(d) depicts the equivalent circuit (EC) model of the structure. Each ring is modeled using a combination of inductors (L) and capacitors (C) to represent its electromagnetic behaviour. The gold rings (Rings 1 and 2) are modeled with corresponding LC resonators (L_1C_1 and L_2C_2), while the graphene rings (Rings 3 and 4) are represented by tunable resonant branches (L_3C_3 and L_4C_4), capturing the graphene-induced plasmonic effects. The parallel connection of these resonators' mimics the overall absorber behaviour, where the combined impedance is engineered to match free space impedance ($Z_0 \approx 377\ \Omega$). This equivalent circuit model not only validates the electromagnetic simulation but also provides physical insight into the resonance mechanism.

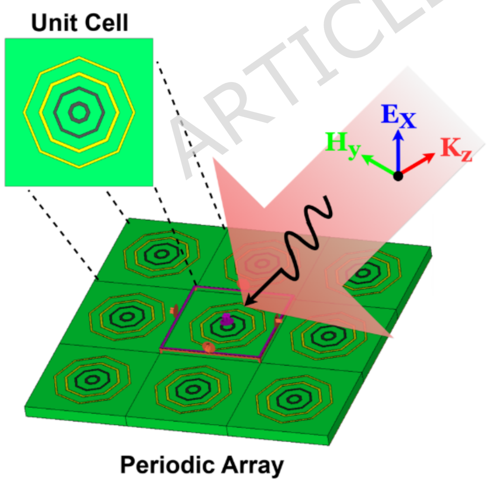

(12)

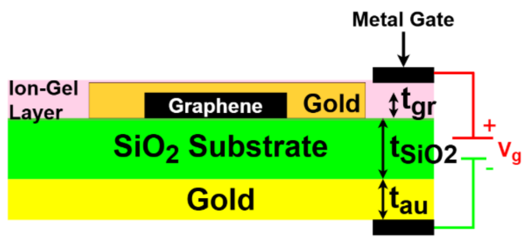

(b)

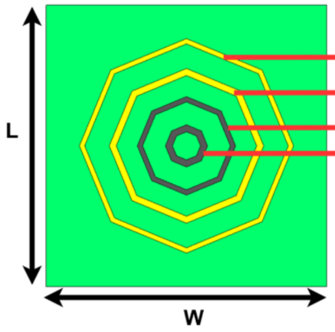

(c)

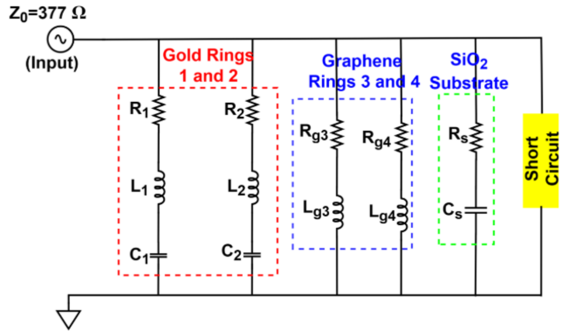

(d)

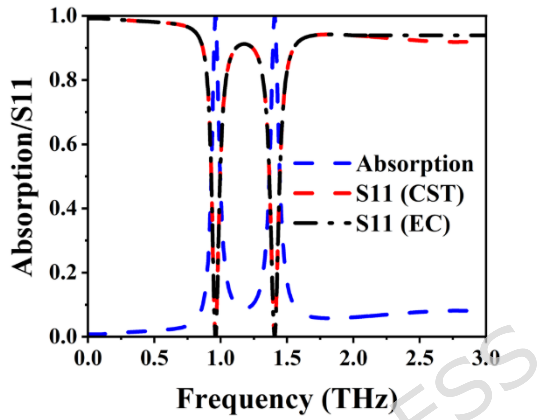

(e)

Fig. 1. Proposed Absorber: (a) Periodic structure, (b) Front View, (c) Unit Cell, (d) Equivalent Circuit (EC), and (e) Frequency Response.

Fig. 1(e) shows the frequency response of the proposed absorber, comparing the absorption spectrum with the simulated S_{11} (CST) and S_{11} (Equivalent Circuit) results. The absorption peaks in the terahertz range closely align with the dips in S_{11}, confirming excellent agreement between CST simulations and the circuit model. The strong absorption indicates that the structure achieves near-perfect impedance matching, while the multi-resonant nature of the design arises from the hybrid gold–graphene ring configuration. To ensure accuracy, the design optimization was carried out using CST Microwave Studio with the frequency-domain solver (FDS). A mesh resolution of 122 cells per wavelength was applied, resulting in 199,657 tetrahedrons for precise computation. This fine meshing ensured convergence of results and minimized numerical errors, validating the structural performance. To better understand the physical mechanism behind the dual-band absorption, the design is interpreted using an equivalent circuit model (EC). The four-ring metamaterial is modeled as four parallel branches interacting with the incoming THz wave. Each gold ring (rings 1 and 2) is represented by a series R–L–C resonator, since metallic rings store energy in both magnetic (inductive) and electric (capacitive) forms, while also exhibiting finite ohmic and radiative losses. Each graphene ring (rings 3 and 4) is represented as a series R–L branch, dominated by conductive response with kinetic inductance. The graphene branches are placed in parallel with the respective gold resonators they couple to. Physically, the gold rings determine the two resonance frequencies (dual-band operation), whereas the graphene primarily enhances dissipative loss near those resonances, improving impedance matching with free space and increasing absorption toward unity. Because the resistance of graphene (▯▯) is much larger than the resistance of gold (▯), the resonance frequencies remain governed by the gold RLC rings. Tthe substrate is represented by a parallel branch composed of a capacitance C_s and a resistance R_s. The capacitance arises due to dielectric loading, and can be approximated by the parallel-plate expression:

$$C_s = \frac{\varepsilon_0 \varepsilon_r A}{t_{SiO2}} \tag{1}$$

where ε_0 is the vacuum permittivity, ε_r=2.25 is the relative permittivity of SiO_2, A=80 μm×80 μm is the unit cell area, and ts is the substrate thickness. For ts≈9 μm, this yields Cs≈63 fF. The corresponding dielectric loss is modeled as:

$$R_s \approx \frac{1}{\omega C_s \tan\delta} \tag{2}$$

with tan δ≈0.001 for SiO_2 at THz frequencies, giving $R_s \approx 2.5$ kΩ. This large resistance indicates the substrate introduces negligible loss compared to metal and graphene.

At the same time, the graphene branches introduce additional frequency-dependent admittance that suppresses reflection without significantly shifting the resonance positions. This behavior is quantitatively described by the branch impedances:

For a gold branch (series R–L–C):

The complex impedance of a gold branch (series R–L–C) is given by equation (3):

$$Z_{gold}(j\omega) = R + j\omega L + 1/j\omega C \tag{3}$$

The complex impedance of the graphene branch (Series R-L) is given by equation (4) [38]:

$$Z_{graphene}(j\omega) = R_g + j\omega L_g \tag{4}$$

The complex impedance of the substrate branch is given by:

$$Z_{sub}(j\omega) = \frac{1}{j\omega C_s} \parallel R_s$$

The total admittance seen by the incoming wave is

$$Y_{tot}(j\omega) = {}^{1}\!/_{Z_1} + {}^{1}\!/_{Z_2} + {}^{1}\!/_{Z_{g3}} + {}^{1}\!/_{Z_{g4}} + {}^{1}\!/_{Z_{sub}} \quad (5)$$

The equivalent input impedance is $Z_{eq}(j\omega) = 1/Y_{tot}(j\omega)$.

The reflection coefficient with respect to free-space impedance (Z_0=377 Ω) is

$$\Gamma(\omega) = \frac{Z_{eq}(\omega) - Z_0}{Z_{eq}(\omega) + Z_0} \quad (6)$$

Finally, since the absorber employs a metallic ground plane to eliminate transmission, absorption is given by:

$$A(\omega) = 1 - |\Gamma(\omega)|^2 \quad (7)$$

For the target dual-frequency operation at 0.9623 THz and 1.4079 THz, the circuit parameters were optimized. The gold rings were modeled with inductances and capacitances of L_1=40 pH, C_1=0.7017 fF (lower frequency), and L_2=30 pH, C_2=0.4459 fF (higher frequency). The series resistances representing ohmic and radiative losses were set as R_1=0.8 Ω and R_2=0.9 Ω. The graphene rings were modeled with higher resistances and small kinetic inductances: R_{g3}=150 Ω, L_{g3}=8 pH (enhancing the first resonance) and R_{g4}=180 Ω, L_{g4}=6 pH (enhancing the second resonance). These values ensure that the gold rings set the resonant frequencies, while the graphene branches introduce controlled dissipative loading. The resulting equivalent circuit improves free-space impedance matching, thereby pushing the absorption peaks close to unity. This agreement between the physical design and circuit-level interpretation validates the absorber's dual-band performance.

III. Evolution of the absorber

The performance of the proposed absorber was systematically studied by incrementally adding metallic and graphene rings to understand their contributions to absorption enhancement. Figure 2 illustrates this step-by-step evolution. Figure 2(a) shows the response of the absorber when only a single gold ring (Ring 1) is present. In this case, the structure resonates at 0.9787 THz with a peak absorption of 0.9625. This indicates that a single metallic resonator is capable of supporting a fundamental resonance, but the absorption is not yet maximized.

When a second gold ring (Ring 2) is introduced, as shown in Figure 2(b), the absorber begins to exhibit a dual-band response. Resonances are observed at 1.434 THz with a peak absorption of 0.9637. The introduction of Ring 2 introduces additional capacitive and inductive coupling, enabling the absorber to operate over multiple resonant frequencies. However, the absorption strength at both resonances remains slightly limited due to insufficient impedance matching with free space.

The incorporation of graphene Ring 3, shown in Figure 2(c), significantly enhances the absorption characteristics. With this addition, the absorber demonstrates improved impedance matching due to the resistive and kinetic inductive contribution of graphene. The resulting peak absorption values increase to 0.9848 at 0.9758 THz and 0.9995 at 1.4224 THz. This improvement clearly highlights the role of graphene in introducing controlled dissipative losses that optimize absorption without shifting the resonance positions dominated by the gold rings.

Finally, the proposed configuration, shown in Figure 2(d), includes both gold rings (Rings 1 and 2) and both graphene rings (Rings 3 and 4). This optimized design exhibits nearly perfect absorption, achieving 0.9998 at 0.9623 THz and 0.9995 at 1.4079 THz. The presence of the second graphene ring further strengthens admittance at both resonant frequencies, pushing the absorption peaks very close to unity and ensuring excellent impedance matching.

An additional advantage of introducing graphene is its tunability via the chemical potential (μ_c). By varying μ_c through electrostatic gating or chemical doping, the surface conductivity of graphene can be dynamically controlled. This, in turn, adjusts the effective admittance of the graphene branches, allowing post-fabrication tuning of absorption strength and bandwidth. Such tunability provides flexibility for real-time reconfiguration of the absorber, making it highly suitable for practical terahertz sensing and communication applications.

Thus, the stepwise evolution from a single metallic resonator to the final hybrid gold–graphene configuration clearly demonstrates the role of gold in defining the resonant bands and graphene in enhancing and tuning absorption, culminating in the proposed absorber with near-unity performance at dual frequencies.

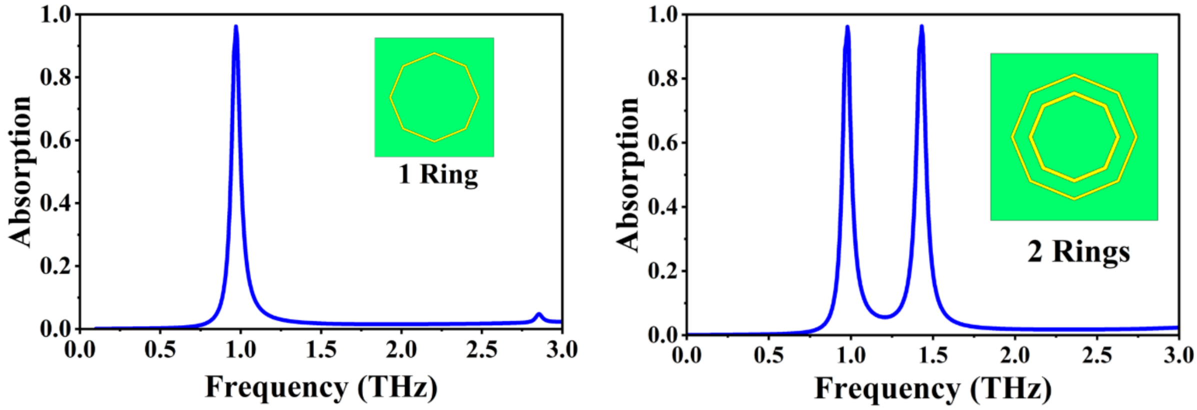

(a) (b)

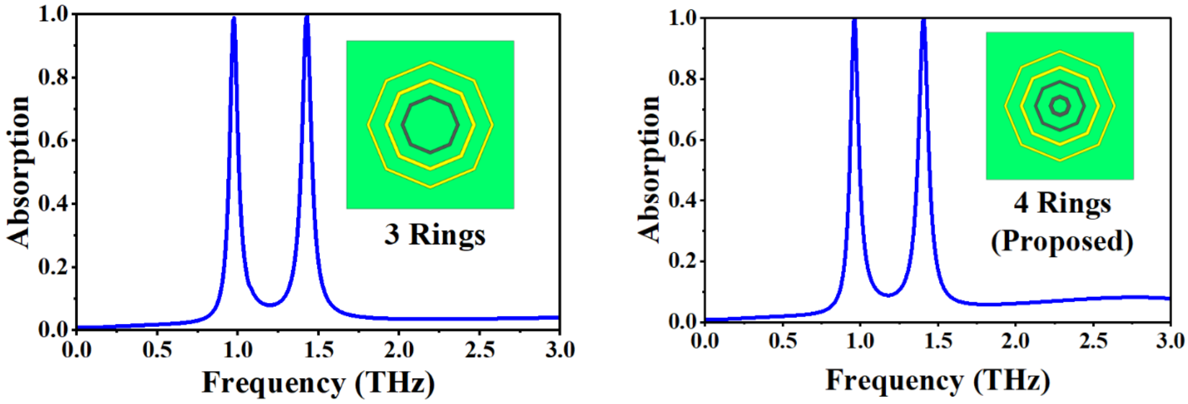

(c) (d)

Fig. 2. Evolution of the absorber: (a) 1 Ring, (b) 2 Rings, (c) 3 Rings, (d) 4 Rings (Proposed).

IV. Parametric Variation

To optimize the absorber, a systematic parametric study was performed where only one parameter was varied at a time while keeping others constant. Each case also includes the electric field distribution, which validates the observed absorption behavior as depicted in Figure 3. The analysis provides insight into the physical mechanisms behind the observed resonances and helps identify the best dimensions for near-unity absorption. Initially, the substrate thickness (t_{sio2}) was varied from 7 μm to 11 μm in steps of 1 μm as shown in Figure 3(a). At t_{sio2} = 9 μm, the absorber achieves nearly perfect absorption of 0.99986 at 0.9623 THz and 0.99992 at 1.4079 THz. The electric field distribution shows strong confinement at this thickness, indicating excellent impedance matching with free space. At smaller (7 μm, 8 μm) or larger values (10 μm, 11 μm), the absorption slightly decreases because the effective optical path length shifts the resonance condition, leading to minor impedance mismatch. Next parameter considered was the outer radius of Ring 1, r_{o1}, varied from 29 μm to 31 μm. The best performance occurs at r_{o1} = 30 μm, where the structure exhibits maximum absorption at both resonances as depicted in Figure 3(b). This is because the outer radius directly governs the inductive–capacitive balance of the fundamental resonance. Any deviation from 30 μm either reduces the coupling efficiency or shifts the resonance away from the designed band, lowering the absorption. Similarly, the inner radius of Ring 1, r_{i1}, was varied between 27 μm and 29 μm, with the optimum at 28 μm as shown in Figure 3(c). At this value, the field distribution confirms stronger confinement inside the ring, which enhances absorption. When the value is smaller or larger than 28 μm, the geometric symmetry and effective capacitance are altered, leading to less efficient resonance coupling and reduced absorption.

In the following case, the outer radius of Ring 2, r_{o2}, was varied from 21 µm to 23 µm. The maximum absorption is achieved at 22 µm, where the resonance condition aligns perfectly with the target bands as depicted in Figure 3(d). At 21 µm or 23 µm, slight detuning reduces absorption strength because the stored electric and magnetic energies do not balance optimally. The next parameter studied was the inner radius of Ring 2, r_{i2}, varied between 19 µm and 21 µm as depicted in Figure 3(e). The highest absorption occurs at 20 µm, which provides the correct capacitive gap and inductive loop size for strong resonance. At other values, either the ring becomes too narrow, increasing resistance and lowering the Q-factor, or too wide, shifting capacitance and resonance frequency, leading to weaker absorption.

Continuing with Ring 3, its outer radius r_{o3} was adjusted from 13 µm to 15 µm, with the optimum value being 14 µm as depicted in Figure 3(f). This dimension ensures strong coupling between the gold and graphene rings, thereby enhancing absorption at both bands. At 13 µm or 15 µm, the resonance becomes slightly misaligned due to changes in the loop inductance, which results in lower confinement and reduced absorption. Following this, the inner radius of Ring 3, r_{i3}, was varied between 11 µm and 13 µm, with the optimum performance observed at 12 µm as depicted in Figure 3(g). At this point, the resonance condition is satisfied precisely, giving near-unity absorption. Smaller values increase capacitance and shift the resonance away, while larger values reduce field confinement, both cases leading to weaker absorption efficiency.

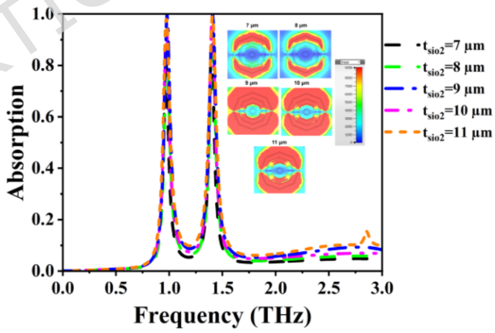

(a)

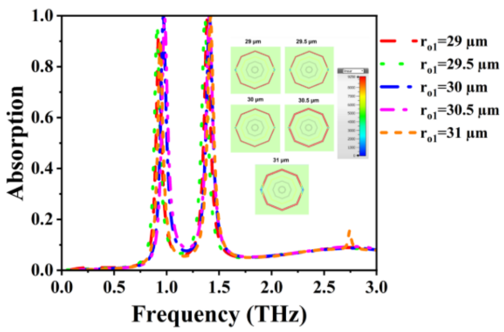

(b)

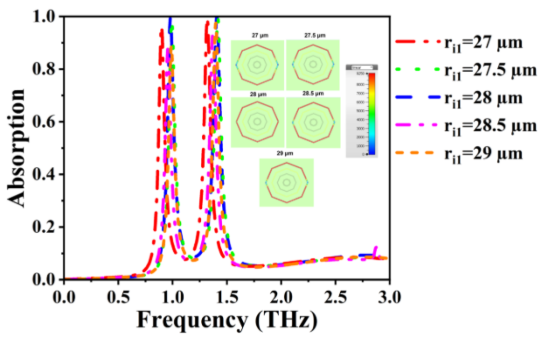

(c)

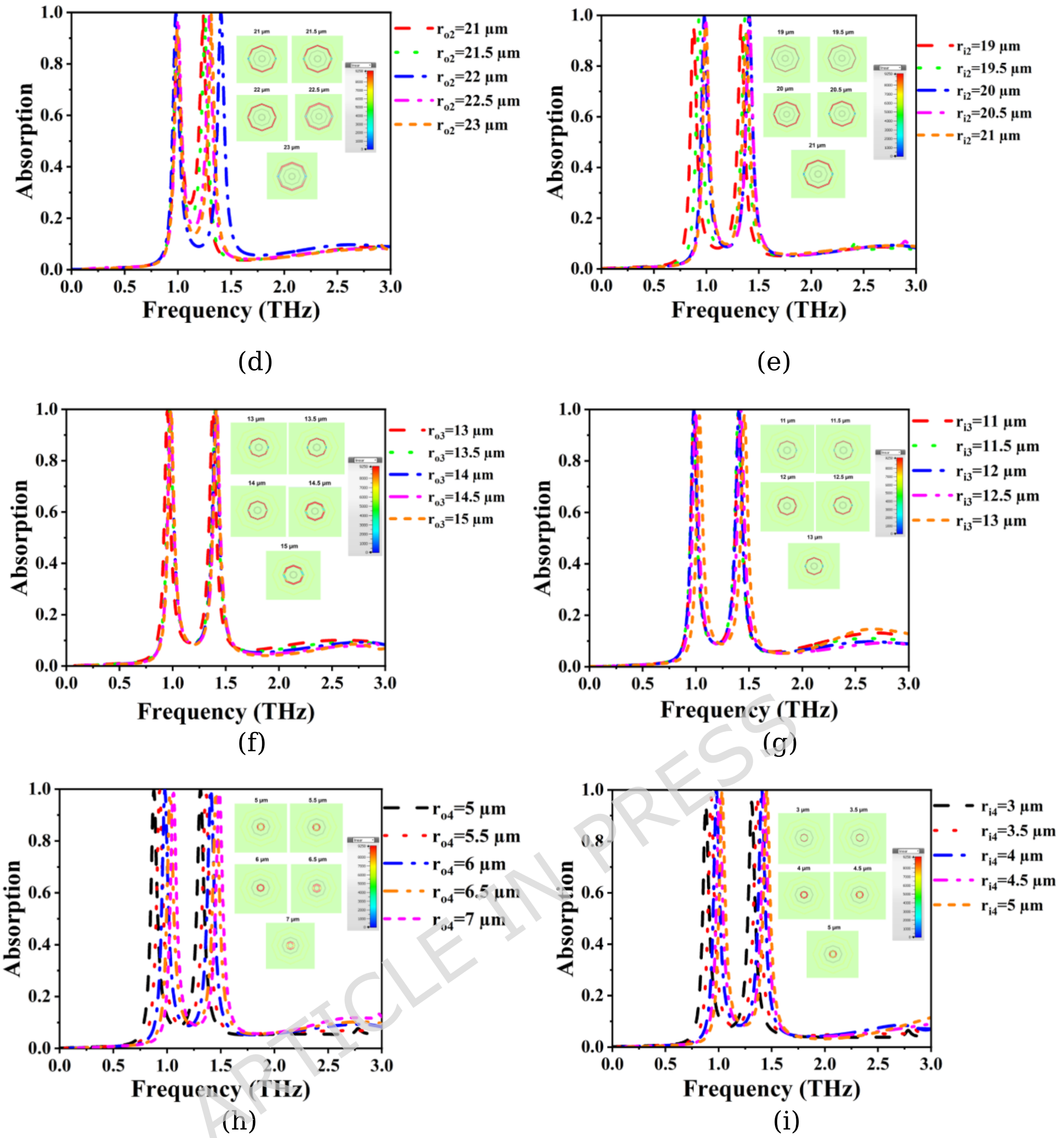

Fig. 3. Parametric Analysis: (a) t_{sio2}, (b) r_{o1}, (c) r_{i1}, (d) r_{o2}, (e) r_{i2}, (f) r_{o3}, (g) r_{i3}, (h) r_{o4}, and (i) r_{i4}.

Next, the outer radius of Ring 4, r_{o4}, was varied between 5 μm and 7 μm, with the best result at 6 μm as depicted in Figure 3(h). At this size, the absorber shows strong localized electric fields in the graphene ring, boosting absorption at both resonances. At smaller or larger values, detuning occurs due to mismatched inductive loading, which slightly decreases the absorption strength. Finally, the inner radius of Ring 4, r_{i4}, was varied from 3 μm to 5 μm, where the optimum occurs at 4 μm as depicted in Figure 3(i). The electric field distribution at this value shows maximum concentration in the graphene region, confirming strong coupling. At 3 μm or 5 μm, the capacitance is disturbed, which reduces the absorption performance.

In all cases, the optimum parameter set (t_{sio2} = 9 μm, r_{o1} = 30 μm, r_{i1} = 28 μm, r_{o2} = 22 μm, r_{i2} = 20 μm, r_{o3} = 14 μm, r_{i3} = 12 μm, r_{o4} = 6 μm, r_{i4}

= 4 μm) ensures strong field confinement and excellent impedance matching with free space, giving rise to near-unity absorption. In contrast, deviations from these values disturb the resonant balance of inductance and capacitance, causing slight impedance mismatch and reduced absorption efficiency.

V. Stability Analysis and Tunability

The absorber exhibits polarization-independent behavior due to the inherent symmetry of its geometry. As shown in Fig. 4(a), the absorption spectra under both TE and TM polarizations demonstrate nearly identical responses, ensuring robustness against variations in polarization states of the incident wave. This characteristic is particularly beneficial for practical applications, where incident waves often encounter arbitrary polarization. Further analysis of angular stability is presented in Fig. 4(b) and Fig. 4(c) for TE and TM incidences, respectively. Under TE incidence, the absorber maintains an absorption above 90% for incidence angles up to approximately 70°, after which the performance shows a gradual decline. Similarly, under TM incidence, the structure sustains an absorption above 90% for angles up to 60°, beyond which the efficiency decreases. These results confirm that the designed absorber maintains a strong and stable resonance response over a wide angular range. The combination of polarization insensitivity and high angular tolerance underscores the robustness of the proposed design, making it highly suitable for terahertz sensing and communication applications where signals often impinge from multiple directions and polarization states.

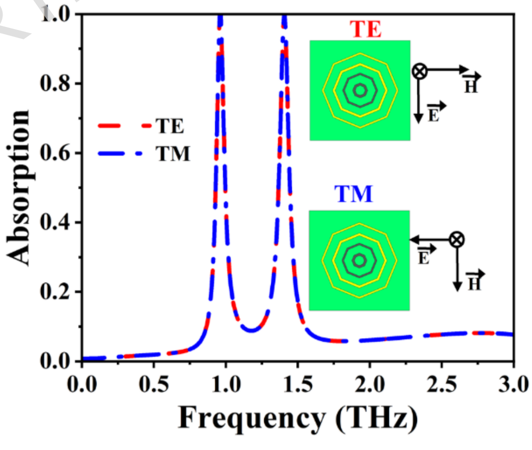

(a)

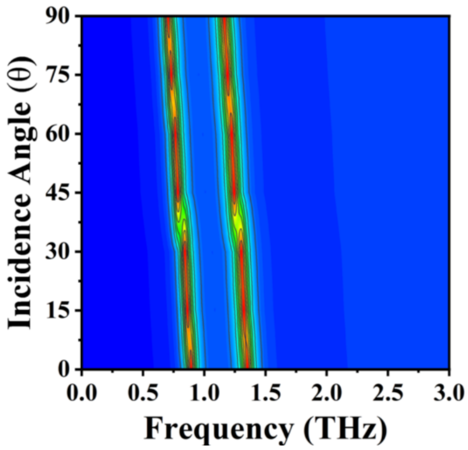

(b)

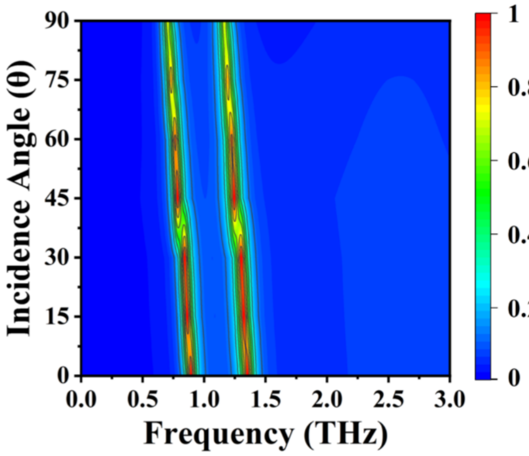

(c)

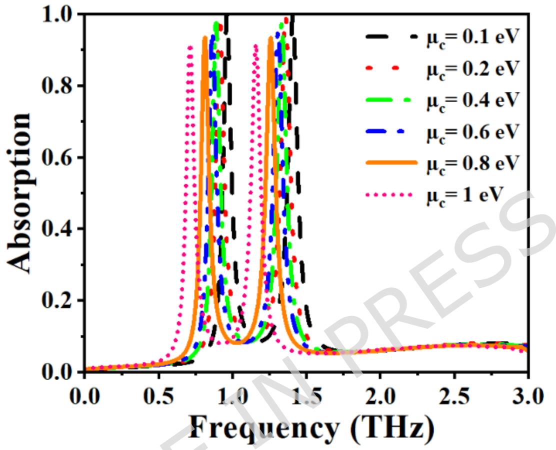

(d)

Fig. 4. Polarization and angular response: (a) Absorption under TE and TM polarizations. Angular Stability for (b) TE incidence, (c) TM Incidence, and (d) Graphene's Tunability.

Graphene is a two-dimensional sheet of carbon atoms arranged in a honeycomb lattice, exhibiting exceptional electrical and optical properties that make it a promising material for terahertz and infrared applications. In this work, graphene is modeled in CST using the surface impedance approach derived from the Kubo formalism, where its interaction with electromagnetic waves is governed by its surface conductivity (σ_G). For numerical stability in the solver, an equivalent thickness of 1 nm is assigned. This value does not represent a physical volumetric thickness, but serves as a computational layer that preserves graphene's intrinsic 2D conductive behavior. Accordingly, the graphene rings in the proposed structure are defined geometrically by width for layout purposes, yet they function electrically as thin conductive sheets characterized by surface impedance, rather than as bulk micrometer-thick metallic conductors [39], [40], [41]. Graphene's surface conductivity, $\sigma_G(\omega)$, is commonly modeled through the Kubo formalism as the sum of intraband and interband contributions:

$$\sigma_G(\omega) = \sigma_{intra}(\omega) + \sigma_{inter}(\omega) \tag{8}$$

The intraband (Drude) term is given by:

$$\sigma_{intra}(\omega) = \frac{2e^2 k_b T}{\pi\hbar^2(\omega+i/T)} \ln\left[2\cosh\frac{\mu_c}{2k_B T}\right] \tag{9}$$

The interband contribution is expressed by:

$$\sigma_{inter}(\omega) = \frac{e^2}{4\hbar}\left[\frac{1}{2} + \frac{1}{\pi}\arctan\left(\frac{\hbar\omega-2\mu_c}{2k_B T}\right) - \frac{i}{2\pi}\ln\frac{(\hbar\omega+2\mu_c)^2}{(\hbar\omega-2\mu_c)^2+(2k_B T)^2}\right] \tag{10}$$

Here, the parameters are defined as follows: e is the elementary charge, $\hbar$ is Planck's constant divided by 2π, and k_B represents the Boltzmann constant.

At THz frequencies, the intraband contribution is typically dominant, reflecting the strong free-carrier response of graphene. In contrast, the interband term becomes increasingly important at higher frequencies due to interband transitions. By varying the chemical potential μ_c, one can actively tune the balance between these two contributions. This tunability allows precise adjustment of absorption strength, bandwidth, and resonance position, thereby making graphene an excellent platform for reconfigurable absorbers and multifunctional devices in the THz regime. Figure 4(d) illustrates the tunable absorption characteristics of the proposed absorber by varying the chemical potential (μ_c) of graphene from 0.1 eV to 1.0 eV. A clear trend is observed: as μ_c increases, the resonance peaks shift progressively towards lower frequencies. This behaviour arises from the fundamental electronic properties of graphene, where the surface conductivity is strongly dependent on its chemical potential. An increase in μ_c enhances the carrier concentration in graphene, thereby increasing its plasmonic activity. This results in stronger light–matter interaction and modifies the effective refractive index experienced by the incident terahertz waves. Consequently, the resonance condition is satisfied at longer wavelengths (lower frequencies), leading to a redshift in the absorption spectrum. This dynamic tunability highlights one of the most compelling advantages of integrating graphene into metamaterial absorbers. Unlike conventional materials with fixed electromagnetic properties, graphene allows real-time control over the resonance characteristics through external biasing. Such reconfigurability enables the absorber to adapt to varying operational requirements, making it highly suitable for multifunctional terahertz sensing, modulation, and communication systems.

VI. Field Distribution

The surface current distribution of the proposed absorber at the two operating frequencies is illustrated in Fig. 5. At 0.95 THz, as shown in Fig. 5(a), the current vectors on the bottom gold layer form a distinct circular loop beneath the region corresponding to the outer metallic ring. This strong inductive circulation indicates that the first resonant mode is primarily governed by the excitation of the outer gold ring (Ring 1). A similar observation is made in Fig. 5(b), where the surface current density is concentrated along the periphery of the outer ring. The strong confinement of current around Ring 1 confirms that the absorption peak at 0.95 THz originates from this resonator. Furthermore, the adjacent graphene ring (Ring 3) contributes additional loss, which improves impedance matching and elevates the absorption peak. At the second resonant frequency of 1.376 THz, the surface currents display a different distribution, as depicted in Figs. 5(c) and 5(d). On the bottom gold sheet (Fig. 5(c)), the current loops are observed to be more localised towards the centre of the structure, corresponding to the position of the inner metallic ring (Ring 2). This indicates that the resonance at 1.376 THz is mainly associated with the excitation of Ring 2. In Fig. 5(d), the surface current density is concentrated predominantly along Ring 2, with complementary contributions from the adjacent graphene ring (Ring 4). This configuration results in tighter field confinement near the central region of the unit cell, thereby enhancing the absorption peak. Thus, the surface current distributions validate that the two resonant frequencies are attributed to distinct resonating elements, i.e., the outer ring pair (gold + graphene) at 0.95 THz and the inner ring pair at 1.376 THz. While the gold rings govern the primary resonances, the graphene rings act as auxiliary lossy components that suppress reflections and improve impedance matching, ultimately leading to near-unity absorption at both bands.

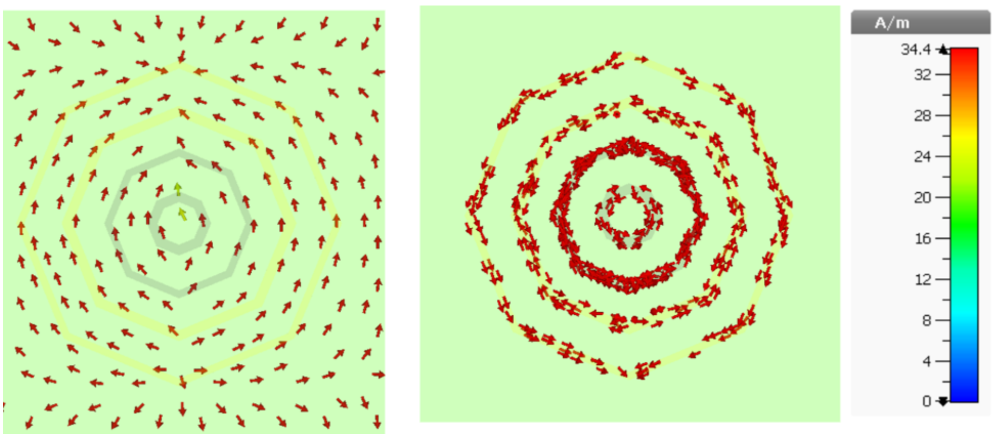

(a) (b)

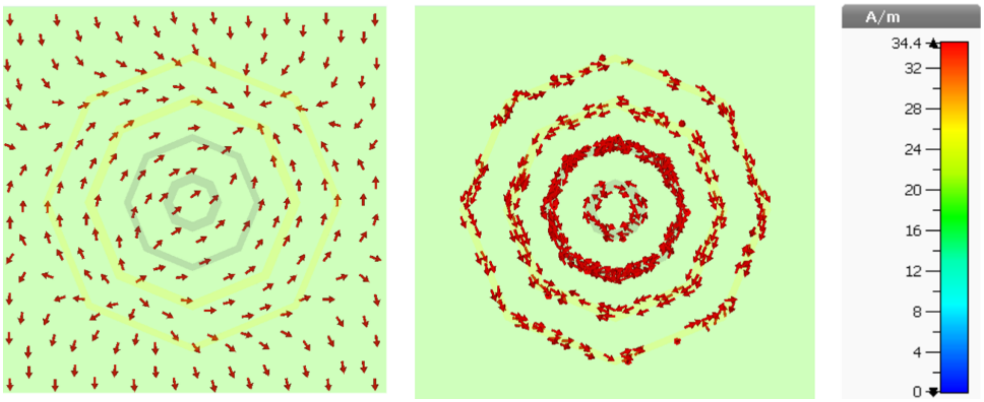

(c) (d)

Fig. 5. Surface current distribution at (a, b) 0.95 THz and (c, d) 1.376 THz, showing currents on the bottom gold plane (a, c) and the top resonator plane (b, d).

VII. Machine Learning Models

Machine learning (ML) has emerged as a powerful tool to accelerate both the design and optimisation of THz absorbers and biosensors. Instead of relying solely on computationally expensive full-wave simulations, ML models trained on simulated or experimental datasets can efficiently forecast critical performance indicators such as absorption, sensitivity, and figure of merit. In the context of biosensing, ML algorithms are particularly advantageous, as they can identify subtle spectral shifts induced by biomolecular interactions with a higher degree of accuracy. This capability not only improves detection reliability but also facilitates adaptive control of device behaviour for either broadband or narrowband operation, depending on the application. Building on these strengths, the present work integrates ML-driven prediction and optimization with a compact, tunable, and switchable absorber configuration, enabling multifunctional THz biosensing with superior efficiency [42], [43], [44], [45], [46], [47]. ML techniques are broadly classified into supervised learning, where models learn from labelled data to predict outcomes, unsupervised learning, which uncovers hidden structures in unlabelled data, and reinforcement learning, where agents optimize decisions through feedback from dynamic environments. In this work, four supervised machine learning algorithms were employed to model and predict the absorption response: Linear Regression (LR), Random Forest (RF), Gradient Boosting (GB), and Support Vector Regressor (SVR). Each of these models operates on a distinct mathematical principle, providing complementary insights into the relationship between structural parameters and absorption.

LR served as the baseline model. It assumes that the target variable can be expressed as a linear combination of the input features x_i, following the formulation

$$y = \beta_0 + \sum_{i=1}^{n} \beta_i x_i + \epsilon \tag{11}$$

Here β_i are the regression coefficients and ϵ is the error term. While LR is easy to interpret and computationally efficient, its inherent assumption of linearity limits its capacity to capture the highly non-linear dependencies in electromagnetic absorption, as reflected in its low R^2 score.

RF, an ensemble method, mitigates the limitations of linearity by aggregating the outputs of multiple decision trees. Each tree is trained on a random subset of the training data and features, and the final prediction is obtained through averaging:

$$\hat{y} = 1/T \sum_{t=1}^{T} h_t(x) \tag{12}$$

where T denotes the number of trees and $h_t(x)$ is the prediction of the t^th^ tree. This randomization strategy reduces variance and prevents overfitting while allowing the model to capture complex feature interactions, leading to significantly improved performance.

GB further refines ensemble learning by building trees sequentially, with each learner trained to minimise the residual errors of its predecessors. The additive model is expressed as

$$F_m(x) = F_{m-1}(x) + \eta h_m(x) \tag{13}$$

where $F_m(x)$ is the boosted model after m iterations, $h_m(x)$ is the weak learner, and η is the learning rate. By focusing on error correction in each stage, GB progressively improves accuracy and generalisation. In this study, GB achieved the highest predictive performance, reflecting its ability to capture intricate non-linear dependencies within the dataset.

Support Vector Regressor (SVR) represents a kernel-based approach that attempts to fit a regression function within a margin of tolerance ϵ. Its regression function can be expressed as

$$f(x) = \sum_{i=1}^{N} \left(\propto_i - \propto_i^* \right) K(x_i, x) + b \tag{14}$$

where $\propto_i$, $\propto_i^*$ are Lagrange multipliers, $K(x_i, x)$ is the kernel function (radial basis function in this case), and b is the bias term. SVR is particularly effective in modelling non-linear relationships by projecting the data into a higher-dimensional space. However, compared to tree-based ensembles, its performance here was moderate, suggesting that the dataset's structure favoured ensemble learning methods.

The predictive performance of the four machine learning models is summarised in Table 1, where R^2, RMSE, and MAE were considered as evaluation metrics. A clear distinction can be observed between the outcomes of linear and non-linear approaches. The Linear Regression (LR) model resulted in a very low R^2 value of around 0.11, with relatively high error values. This indicates that absorption behaviour cannot be sufficiently explained through a simple linear relationship between the structural parameters and the output. Such poor performance is expected, since electromagnetic absorption is inherently governed by highly non-linear and multi-parametric interactions that linear models are not designed to capture. By contrast, the Random Forest (RF) model provided a significant improvement, achieving an R^2 value of about 0.86 along with much lower RMSE and MAE. The ensemble averaging mechanism in RF allows it to capture complex nonlinear dependencies and interactions between features, leading to robust predictions. This result demonstrates the effectiveness of tree-based methods for non-linear datasets, although RF can sometimes be prone to overfitting.

The Gradient Boosting (GB) model further advanced predictive capability, delivering the best performance among the tested algorithms. It reached an R^2 of nearly 0.89 with the lowest RMSE and MAE values. Gradient Boosting's strength lies in its sequential learning process, where each new model focuses on correcting the errors made by the previous ones. This iterative refinement enables the algorithm to identify subtle feature contributions and capture intricate variations in the data. The superior performance of GB highlights its suitability for modelling complex absorption mechanisms. The Support Vector Regressor (SVR) achieved moderate results, with an R^2 of about 0.65 and higher errors compared to the ensemble methods. While SVR is effective in handling non-linear relationships through the use of kernel functions, its performance in this case suggests that it was not as well-suited to capturing the broader range of feature interactions present in the dataset. Nevertheless, SVR still performed better than the purely linear model, confirming its ability to model at least part of the non-linearity. Taken together, these results confirm that tree-based ensemble methods, particularly Gradient Boosting, offer the most reliable and accurate predictive framework for absorption modelling. Linear models are insufficient due to the intrinsic non-linearity of the problem, while kernel methods such as SVR provide intermediate accuracy but do not outperform ensembles in this case. The findings strongly support the application of advanced ensemble techniques in predictive modelling of electromagnetic absorption phenomena.

Table 1. ML Models predictive performance

Model	R^2	RMSE	MAE
Linear Regression	0.109675	0.251581	0.202766
Random Forest	0.862688	0.0988	0.04995
Gradient Boosting	0.865328	0.097846	0.049121
Support Vector Regressor	0.655201	0.156562	0.119818

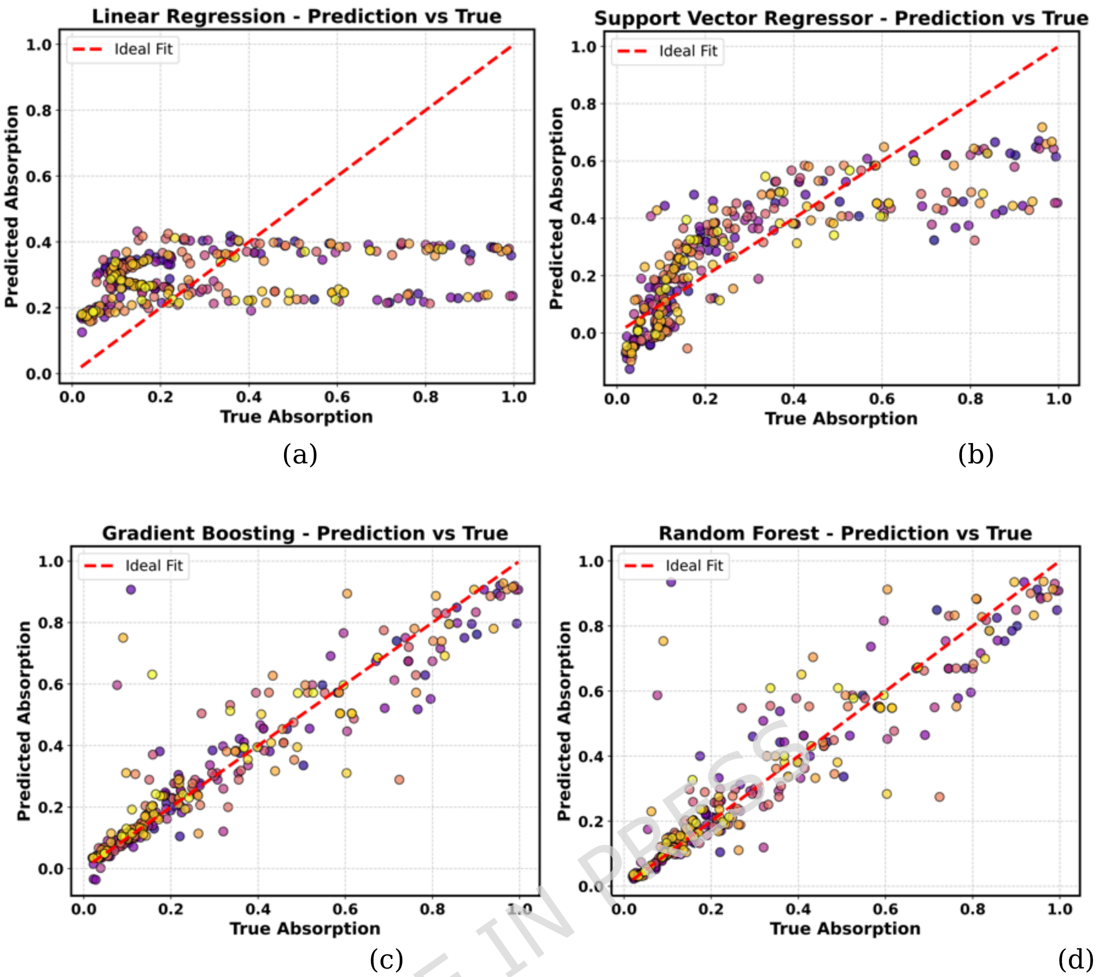

Fig. 6. Absorption: True vs Predicted.

As depicted in Fig. 5, the scatter plots illustrate the relationship between predicted and true absorption values for the four ML models employed. The red dashed line represents the ideal fit, where predicted values perfectly match the true observations. For Linear Regression, the data points show a wide scatter away from the ideal line, indicating that the model is unable to capture the non-linear behaviour of the absorption response. Predictions cluster around lower values, reflecting the limitations of the linear assumption and explaining the low R^2 score. In the case of the Support Vector Regressor, the distribution of points shows an improved alignment with the ideal line compared to Linear Regression, but significant deviations remain, especially at higher absorption values. This suggests that while SVR is capable of modelling some non-linear relationships, it does not fully capture the complex dependencies in the dataset.

The Random Forest and Gradient Boosting models, on the other hand, show a much closer alignment with the ideal fit. In both cases, the majority of points are densely distributed around the diagonal line, demonstrating strong agreement between predicted and true values. Gradient Boosting in particular exhibits the tightest clustering, with minimal scatter, which is consistent with its superior quantitative performance metrics.

VIII. Refractive Index Sensing

The refractive index (RI) sensing performance of the proposed absorber was investigated to demonstrate its applicability for biosensing applications. Owing to its dual-band absorption characteristics with narrow full-width at half maximum (FWHM) values of 0.0682 THz and 0.083 THz, the structure provides strong frequency selectivity, which is essential for the precise detection of small RI variations. As shown in Fig. 7(a), the analyte layer of thickness t_{an} is deposited on top of the device, directly interacting with both the graphene and gold resonating elements. This top-layer placement ensures that even minor changes in the dielectric properties of the analyte strongly perturb the local electromagnetic fields, thereby shifting the resonance positions.

To examine the influence of analyte thickness on sensing performance, Fig. 7(b) presents the frequency shift (FS) for two representative refractive indices, $n = 1.4$ and $n = 1.8$, for both resonant bands. The results show that the FS increases steadily as the analyte thickness t_{an} grows, since a thicker analyte layer enables a larger portion of the resonant near-field to overlap with the sensing region. However, once the thickness reaches approximately $t_{an} \approx 1\ \mu m$, the FS approaches saturation. This behavior indicates that the dominant evanescent field responsible for refractive-index sensing is effectively confined within the first micron above the absorber surface.

The frequency shift is calculated as:

$FS = \frac{f_{t_{an}} - f_{ref}}{f_{ref}} \times 100\%$ where $f_{t_{an}}$ is the resonance frequency for a given analyte thickness and f_{ref} is the reference frequency without the analyte. The saturation trend confirms that increasing the analyte thickness beyond $\sim 1\ \mu m$ does not significantly alter the resonance behavior. Therefore, $t_{an} \approx 1\ \mu m$ is sufficient to achieve optimal sensing performance in the proposed dual-band absorber.

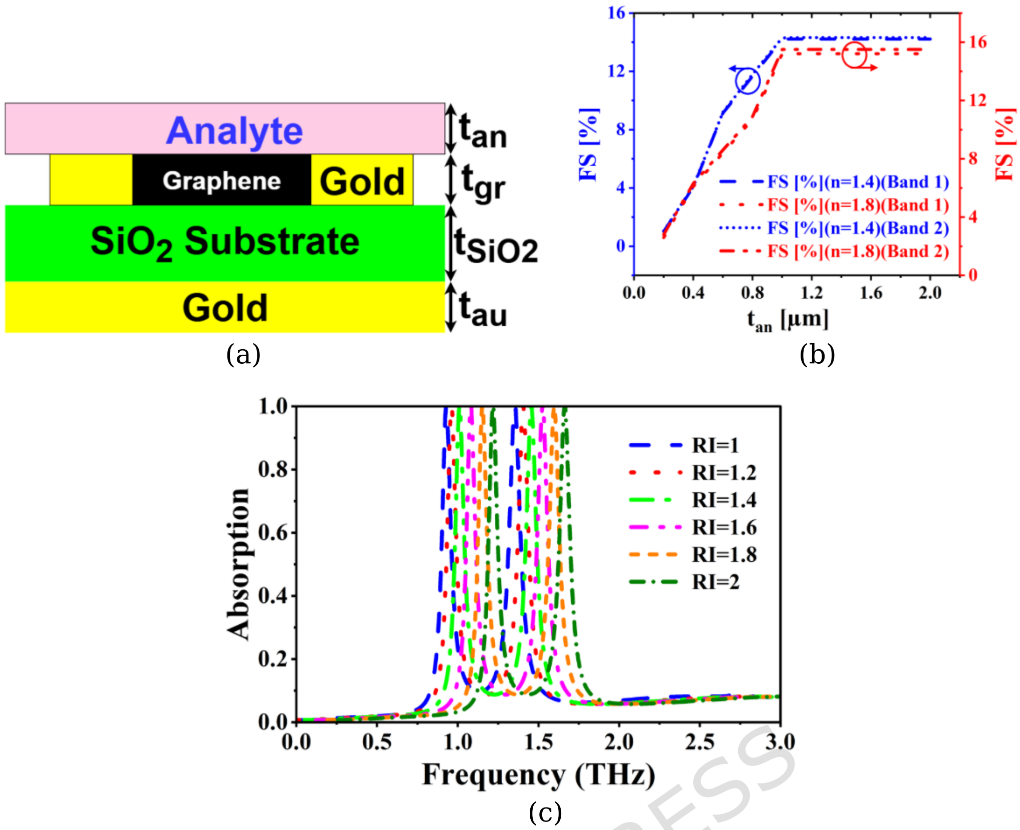

Fig. 7. (a) Analyte, (b) FS vs t_{an}, and (c) Frequency Response.

To evaluate the sensing capability, the refractive index of the analyte was varied systematically from RI = 1.0 to RI = 2.0 in steps of 0.2. The resulting absorption spectra are plotted in Fig. 7(c). It is observed that the resonant peaks undergo a progressive shift towards higher frequencies (blue shift) as the RI of the analyte increases. This frequency shift occurs because a higher refractive index enhances the effective permittivity in the vicinity of the resonators, altering the resonance condition and thereby displacing the absorption bands. Importantly, the dual-band response remains clearly distinguishable for all RI values, reflecting the stability and robustness of the absorber design. The sensitivity of the structure is inherently tied to the strong field confinement within the resonant rings, which makes the device highly responsive to variations in the surrounding dielectric medium. The combination of sharp resonances (narrow FWHM), high absorption efficiency, and consistent frequency shifts demonstrates that the proposed absorber is well-suited for biosensing and chemical detection applications. In particular, the ability to track changes in resonant frequencies with different refractive indices confirms its potential as a reliable platform for detecting different viruses, biological analytes, including pathogens and biochemical solutions.

This behavior contrasts with the typical redshift in conventional dielectric-loaded THz resonators and originates from the graphene–metal hybrid region, where the analyte-induced variation reduces effective capacitive loading, producing a net increase in resonance frequency.

Fig. 8(a) illustrates the resonance frequency shift (Δf) and the corresponding sensitivity (S) as functions of the refractive index (RI). The resonance shift, defined as the difference between the present and previous resonance frequencies ($\Delta f = f_i - f_{i-1}$), indicates the absorber's responsiveness to RI variation. The shift in Band 1 between RI = 1.2 and RI = 1.4 increases from 0.0067 THz to 0.0487 THz, while Band 2 shows a corresponding change from 8.0×10^{-4} THz to 0.0028 THz. These subtle variations become visually compressed in the full-scale plot of Fig. 8, but the extracted values clearly confirm that both resonances respond to changes in refractive index.

Sensitivity (S), calculated using $S = \Delta f / \Delta RI$, increases for both bands as the RI rises, highlighting effective sensing behaviour. However, Band 1 consistently exhibits higher sensitivity than Band 2, achieving a maximum value of 1.7435 THz/RIU at RI = 2.0, whereas Band 2 records 1.2057 THz/RIU. This confirms that Band 1 is more reactive to RI perturbations, making it suitable for high-resolution detection. Fig. 8(b) shows the variation of full width at half maximum (FWHM) and the figure of merit (FOM) with RI. The FOM, determined as FOM = S / FWHM, quantifies the sensing precision by relating sensitivity to resonance sharpness. The nearly stable FWHM across RI values ensures that the resonance peaks remain well-defined and undistorted. As RI increases, the FOM rises steadily, reaching a maximum of 25.60 RIU^{-1} for Band 1 and 15.19 RIU^{-1} for Band 2 at RI = 2.0, confirming the superior sensing accuracy of Band 1.

Fig. 8(c) presents the quality factor (Q), defined by $Q = f_r$ / FWHM, where f_r is the resonance frequency. Both bands exhibit increasing Q values with RI, indicating progressively sharper resonances. The maximum Q values reach 19.23 for Band 1 and 19.65 for Band 2 at RI = 2.0. Interestingly, although Band 2 has lower sensitivity and FOM, it achieves a slightly higher Q, implying cleaner and narrower resonance peaks — beneficial for stable and repeatable sensing. Therefore, the proposed dual-band absorber demonstrates excellent sensing performance. Band 1 offers the highest sensitivity (1.7435 THz/RIU) and FOM (25.60 RIU^{-1}), while Band 2 provides the highest Q (19.65). This combination of high sensitivity, large FOM, and sharp resonance validates the structure's strong dual-band biosensing capability, enabling accurate, stable, and reliable analyte detection in the terahertz regime.

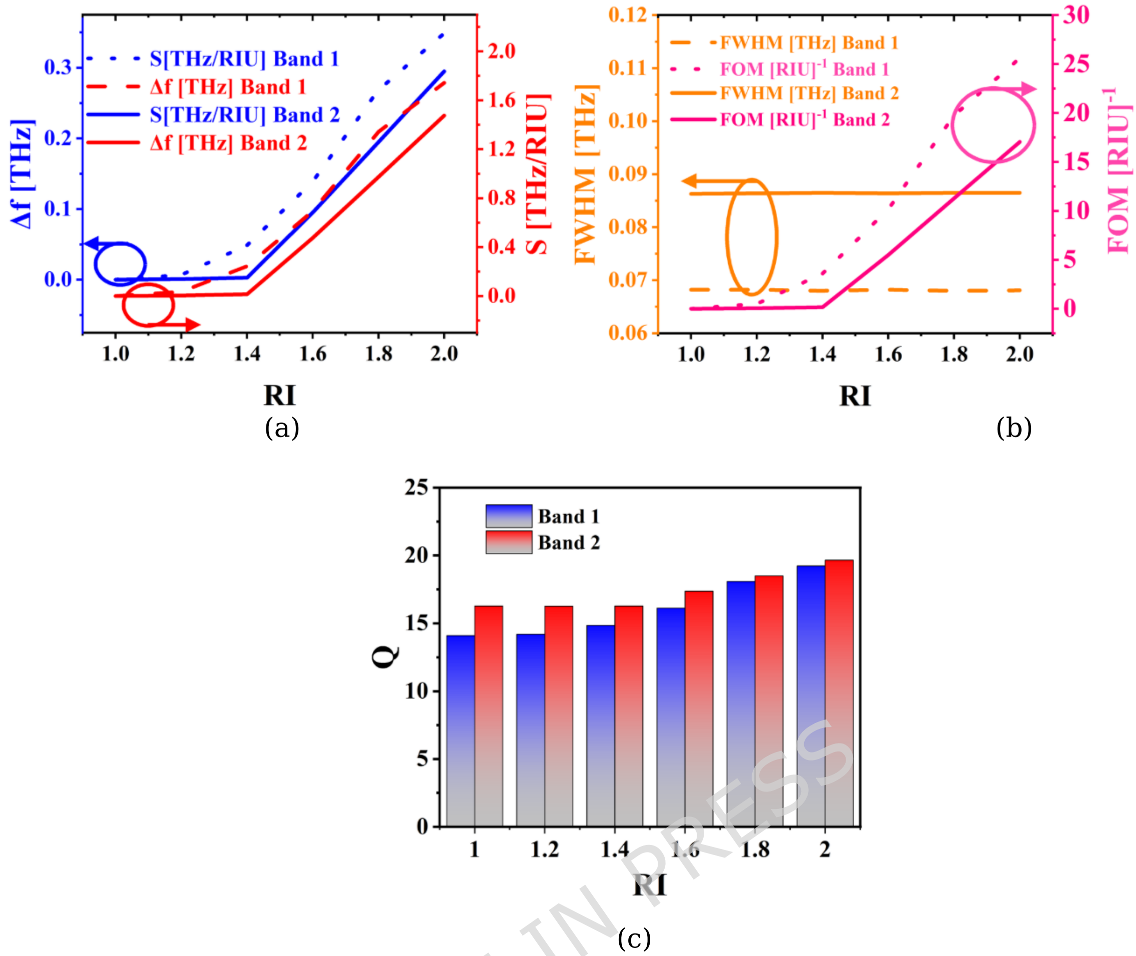

Fig. 8. (a) S, Δf vs RI, (b) FWHM, FOM vs RI, and (c) Q vs RI.

Table 2 presents the sensing performance parameters of the proposed dual-band terahertz absorber for detecting different viruses and cancerous cells. The proposed sensor maintains high and stable performance across various biological analytes. The sensitivity values vary depending on the virus type and refractive index, with the first band exhibiting higher sensitivity in most cases. For example, the breast cancer cell sample shows the maximum sensitivity of 0.1220 THz/RIU in the first band, while the second band achieves a comparable value of 0.1405 THz/RIU for the cervical cancer cell. This demonstrates the absorber's strong dual-band operation and high detection precision for subtle RI variations. The FWHM values remain nearly constant across all analytes, ranging between 0.068–0.0865 THz, which indicates stable and well-confined resonance peaks with minimal spectral distortion. Consequently, the FOM values are consistently high, reaching up to 1.794 RIU^{-1} for the first band (breast cancer cell) and 1.624 RIU^{-1} for the second band (cervical cancer cell). These results confirm that the absorber provides superior sensing accuracy and efficiency in both resonance bands. In terms of resonance sharpness, the quality factor (Q) lies in the range of 14.2–14.8 for the first band and 16.3–16.4 for the second band, reflecting well-defined and narrow absorption peaks. Notably, the second band consistently shows higher Q values, indicating enhanced resonance purity, which is beneficial for precise detection and repeatability.

Thus, Table 2 clearly demonstrates that the proposed dual-band absorber offers robust and consistent sensing performance across different viral and cancerous samples, with high sensitivity, excellent FOM, and strong Q factors. These characteristics highlight its potential for accurate biosensing and early-stage disease identification in terahertz biomedical applications.

Table 2. Sensing Performance for identifying different viruses.

Virus	RI	S		FWHM		FOM		Q	
		1st Band	2nd Band	1st Band	2nd Band	1st Band	2nd Band	1st Band	2nd Band
malaria (n1)	1.373	0.0871	0.1399	0.0682	0.0863	1.277	1.621	14.222	16.303
malaria (n2)	1.383	0.0832	0.1362	0.0682	0.0864	1.221	1.577	14.252	16.307
Dengue	1.4	0.1217	0.1377	0.068	0.0865	1.790	1.592	14.852	16.300
basal cell (cancerous)	1.38	0.0839	0.1373	0.0682	0.0864	1.230	1.589	14.281	16.377
cancer breast cell	1.399	0.1220	0.1308	0.068	0.0865	1.794	1.512	14.852	16.381
cervical cancer cell	1.392	0.0887	0.1405	0.0681	0.0865	1.303	1.624	14.361	16.416
cancerous jurkat	1.39	0.0992	0.1338	0.0681	0.0865	1.457	1.547	14.684	16.439

IX. ML Models for biosensing

The original biosensing dataset was based on limited discrete measurements corresponding to refractive index (RI), resonance frequency shifts, and absorption responses. To enhance the robustness of machine learning (ML) model training, the dataset was systematically expanded by interpolating the measured values and introducing synthetic variations within the realistic physical constraints of the system. This expansion allowed for a larger number of trainings, testing samples, while maintaining the underlying physics of the biosensing mechanism. Consequently, the enriched dataset captures a broader mapping between the input parameters and the output absorption, enabling more accurate model learning and improved generalisation.

Table 3 summarises the predictive performance of four ML models. Linear Regression achieved the highest coefficient of determination (R^2 = 0.994), demonstrating a near-perfect linear mapping between true and predicted absorption values. Its RMSE and MAE values were also the lowest, confirming excellent predictive fidelity. Random Forest showed slightly lower accuracy (R^2 = 0.972) with relatively higher error values (RMSE = 0.201, MAE = 0.161). This indicates that while RF can capture nonlinear interactions, it may have underperformed due to the smooth, physics-driven structure of the dataset. Gradient Boosting achieved strong performance (R^2 = 0.986), outperforming RF and yielding significantly lower error metrics, highlighting its ability to balance bias and variance effectively. Support Vector Regressor also provided robust predictions **(**R^2 = 0.986**)** with errors similar to GB, confirming its strength in handling complex nonlinear relationships in biosensing data. Thus, LR emerged as the best performer due to the inherent linear correlation between RI-induced frequency shifts and absorption changes. Ensemble methods (RF and GB) and kernel-based SVR still provided competitive results, highlighting the complementary roles of linear and nonlinear models in biosensing prediction.

Table 3. ML Models Performance

Model	**R^2**	**RMSE**	**MAE**
Linear Regression	0.993986	0.093404	0.073494
Random Forest	0.972153	0.200992	0.161207
Gradient Boosting	0.986167	0.141661	0.117917
Support Vector Regressor	0.986013	0.142446	0.109215

Figure 9 presents the True vs. Predicted plots for each of the four models. In all cases, the scatter points closely align with the reference diagonal line, confirming strong agreement between actual and predicted absorption values. The LR model displays the tightest clustering around the diagonal, reflecting its superior R^2 score. Both GB and SVR show slightly wider scattering but still maintain high predictive accuracy. RF demonstrates comparatively larger deviations, particularly for extreme values, which explains its reduced error performance.

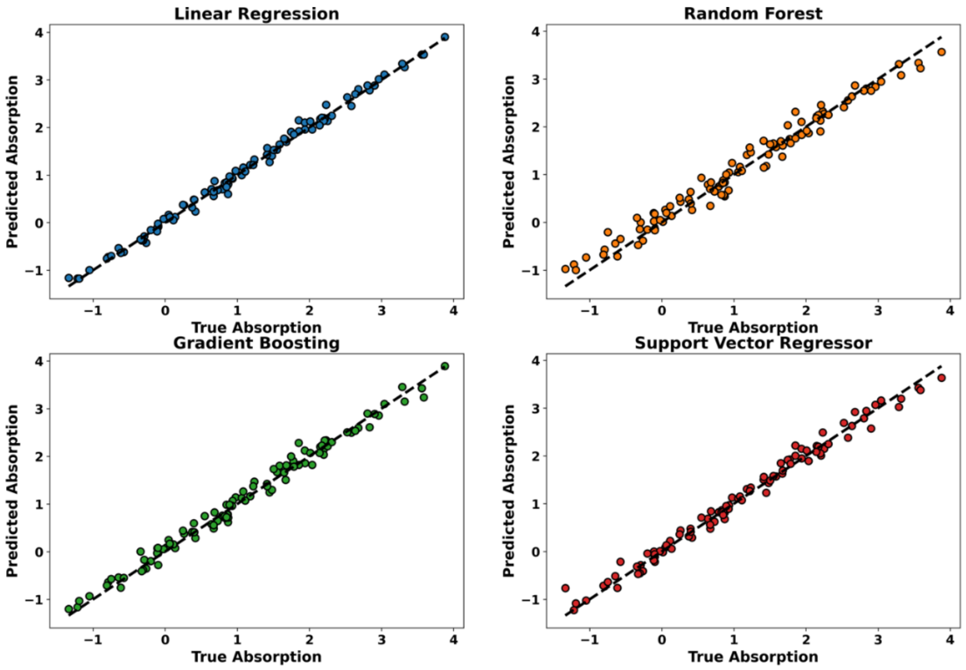

Fig. 9. Biosensing: True vs. Predicted plots.

Two distinct datasets were used for ML analysis in this work. The first dataset models the absorption response based on geometric parameters, which results in a highly non-linear electromagnetic dependency; hence, nonlinear ensemble methods (GB and RF) outperform Linear Regression. In contrast, the biosensing dataset maps absorption/frequency shifts to refractive index, where the response is predominantly linear; therefore, Linear Regression achieves the highest accuracy ($R^2 = 0.994$). These differences reflect inherent physical variations between geometry-dependent EM behavior and RI-driven sensing characteristics

X. Comparison

The comparison presented in Table 4 highlights the performance of various dual-band metamaterial absorbers reported in the literature alongside the proposed design. Most earlier works have successfully demonstrated dual-band absorption, but often at the expense of either limited sensitivity, moderate figure of merit (FOM), or design complexity. For instance, the absorbers in [28], [29], [30], [31], [33] achieve dual-band operation, yet they generally involve intricate geometries that are challenging to fabricate and integrate. Moreover, in many cases, parameters such as polarisation insensitivity (PI) and tunability (Tu) are either not realised or only partially addressed, restricting their practical adaptability. In contrast, the proposed absorber demonstrates significant advancements by achieving near-unity absorption at 0.9623 THz and 1.4079 THz while maintaining high sensitivities of 1.7435 and 1.475 THz/RIU. This directly translates into superior FOM values of 25.6 and 17.05, which are notably higher than those of earlier designs. The quality factors (Q) of 19.23 and 19.65 further confirm its sharp resonances, enabling precise detection capabilities. Importantly, the design maintains a relatively thin profile (9.07 μm), while simultaneously ensuring polarisation insensitivity and tunability. Unlike the complex unit cell arrangements observed in prior works, the proposed absorber achieves this performance with a simpler geometry, making fabrication more straightforward and practical.

Table 4. Comparison with other articles.

Ref	Bands	f (THz)	S (THz/RIU)	FOM (1/RIU)	Q	T (μm)	PI	Tu	Design Method
[33]	2	5.1, 11.7	2.08, 4.72	6.7, 13.88	-	3	no	yes	MM
[31]	2	0.97, 2.88	0.304, 0.912	2.47, 2.49	7.65, 7.87	18	No	yes	MM
[30]	2	0.78, 0.904	0.0515, 0.076	0.86, 1.15	12.8, 13.5	-	no	yes	MM
[29]	2	0.990, 1.632	0.9304	12.53	23.7	50	no	-	MM
[28]	2	1.994, 2.7	0.6, 0.8	3.66, 2.64	12.24, 8.9	-	no	yes	MM
[36]	2	0.89,1.36	0.03	3.3	121.4	250	No	No	MM
[37]	1	1.9656	0.836	9.238	21.711	33.7	yes	yes	MM
Proposed	2	0.9623, 1.4079	1.7435, 1.475	25.6, 17.05	19.23, 19.65	9.07	Yes	Yes	MM

XI. Conclusion

A dual-band, graphene-assisted metamaterial absorber has been designed and optimised for biosensing in the terahertz regime. The combination of gold and graphene rings ensures strong resonant absorption and tunability, achieving near-perfect absorption at two distinct frequencies. The structure not only exhibits superior sensitivity, figure of merit, and quality factor compared to previously reported designs, but also offers compactness and ease of fabrication. Through equivalent circuit modelling and parametric analysis, the absorption mechanism and the effect of geometrical variations were thoroughly explained. Additionally, the integration of machine learning provides a significant advantage by accelerating performance prediction and enhancing biosensing accuracy, particularly for virus detection. Overall, the proposed design bridges the gap between high-performance THz absorbers and intelligent sensing platforms, offering a promising pathway toward practical biomedical and environmental sensing applications.

Acknowledgements

The work was supported by Vellore Institute of Chennai, Tamil Nadu, INDIA.

Author contributions

Shagun Gupta, Vaishnavi Chandrashekar Gosi, Parth Pareek, Patri Upender: Research, Writing, Editing, review, Validation.

Funding

Open access funding provided by Vellore Institute of Technology Chennai.

Declarations

Competing interests

The authors declare no competing interests.

References:

[1] G. P. Williams, “Filling the THz gap—high power sources and applications,” *Reports on Progress in Physics*, vol. 69, no. 2, p. 301, Dec. 2005, doi: 10.1088/0034-4885/69/2/R01.

[2] P. H. Siegel, “Terahertz technology,” *IEEE Trans Microw Theory Tech*, vol. 50, no. 3, pp. 910–928, Mar. 2002, doi: 10.1109/22.989974.

[3] H. J. Song and T. Nagatsuma, “Present and future of terahertz communications,” *IEEE Trans Terahertz Sci Technol*, vol. 1, no. 1, pp. 256–263, Sep. 2011, doi: 10.1109/TTHZ.2011.2159552.

[4] D. W. Porterfield, “High-efficiency terahertz frequency triplers,” *IEEE MTT-S International Microwave Symposium Digest*, pp. 337–340, 2007, doi: 10.1109/MWSYM.2007.380439.

[5] I. F. Akyildiz, J. M. Jornet, and C. Han, “Terahertz band: Next frontier for wireless communications,” *Physical Communication*, vol. 12, pp. 16–32, Sep. 2014, doi: 10.1016/J.PHYCOM.2014.01.006.

[6] M. Gupta and R. Singh, “Terahertz Sensing with Optimized Q/Veff Metasurface Cavities,” *Adv Opt Mater*, vol. 8, no. 16, p. 1902025, Aug. 2020, doi: 10.1002/ADOM.201902025.

[7] D. K. Lee *et al.*, “Nano metamaterials for ultrasensitive Terahertz biosensing,” *Scientific Reports 2017 7:1*, vol. 7, no. 1, pp. 1–6, Aug. 2017, doi: 10.1038/s41598-017-08508-7.

[8] W. Cui, L. Li, W. Xue, H. Xu, Z. He, and Z. Liu, “Enhanced absorption for MXene/Au-based metamaterials,” *Results Phys*, vol. 23, p. 104072, Apr. 2021, doi: 10.1016/J.RINP.2021.104072.

[9] G. Choi *et al.*, “Enhanced Terahertz Shielding of MXenes with Nano-Metamaterials,” *Adv Opt Mater*, vol. 6, no. 5, p. 1701076, Mar. 2018, doi: 10.1002/ADOM.201701076.

[10] J. Wang, Y. Yao, X. Liu, G. Liu, and Z. Liu, "Switchable Wideband Terahertz Absorber Based on Refractory and Vanadium Dioxide Metamaterials," *IEEE Photonics J*, vol. 15, no. 1, Feb. 2023, doi: 10.1109/JPHOT.2023.3234535.

[11] U. Patri and A. Kumar, "THz biosensing for early detection of influenza and coronaviruses using dielectric metamaterials," *Phys Scr*, vol. 99, no. 12, p. 125511, Nov. 2024, doi: 10.1088/1402-4896/AD8B7E.

[12] W. Xu *et al.*, "Terahertz biosensing with a graphene-metamaterial heterostructure platform," *Carbon N Y*, vol. 141, pp. 247–252, Jan. 2019, doi: 10.1016/J.CARBON.2018.09.050.

[13] A. Movahednia, V. Mashayekhi, E. Zareian-Jahromi, and S. M. Hashemi, "Graphene-based metamaterial ultrawideband absorber with enhanced terahertz performance," *Results Phys*, vol. 65, p. 107965, Oct. 2024, doi: 10.1016/J.RINP.2024.107965.

[14] P. Upender and A. Kumar, "Design of a multiband graphene-based absorber for terahertz applications using different geometric shapes," *JOSA B, Vol. 39, Issue 1, pp. 188-199*, vol. 39, no. 1, pp. 188–199, Jan. 2022, doi: 10.1364/JOSAB.440757.

[15] B. Khodadadi, P. Rezaei, and S. Hadipour, "Accurate graphene-based absorber for slight leakage detection of Radon and chloroform air-pollution," *Results Phys*, vol. 71, p. 108196, Apr. 2025, doi: 10.1016/J.RINP.2025.108196.

[16] M. F. Ali, A. Singh, P. Giri, and G. Varshney, "Graphene Supported Ultrathin VO2Resonators for Multifunctional THz Absorption," *IEEE Transactions on Plasma Science*, vol. 52, no. 2, pp. 545–552, Feb. 2024, doi: 10.1109/TPS.2023.3342115.

[17] J. Shen, H. Li, X. Qiu, J. Lu, Y. Wang, and C. Jin, "VO2-Graphene based four-state ultra-wideband terahertz metamaterial with switchable absorption, reflection, and transmission," *Micro and Nanostructures*, vol. 203, p. 208143, Jul. 2025, doi: 10.1016/J.MICRNA.2025.208143.

[18] S. Barzegar-Parizi and Z. Vafapour, "Dynamically Switchable Sub-THz Absorber Using VO2Metamaterial Suitable in Optoelectronic Applications," *IEEE Transactions on Plasma Science*, vol. 50, no. 12, pp. 5038–5045, Dec. 2022, doi: 10.1109/TPS.2022.3224479.

[19] P. Upender, P. Sandeep, S. P. Bharathi, K. Kumba, and A. Kumar, "Advanced VO2-Graphene based compact THz absorber for EM shielding and biosensing applications," *Ain Shams Engineering Journal*, vol. 16, no. 1, p. 103226, Jan. 2025, doi: 10.1016/J.ASEJ.2024.103226.

[20] H. Korkmaz, "MXene-Based Perfect Absorber Design and Refractive Index Sensing Performance," *Plasmonics 2025*, pp. 1–8, Jan. 2025, doi: 10.1007/S11468-025-02791-1.

[21] M. Saqlain, M. A. Baqir, and P. K. Choudhury, "MXene-and Graphene-Assisted THz Metamaterial for Cancer Cells Detection Based on Refractive Index Sensing," *IEEE Trans Nanotechnol*, 2024, doi: 10.1109/TNANO.2024.3458427.

[22] T. Sheheryar, Y. Tian, B. Lv, and L. Gao, "High-sensitivity refractive index based terahertz metasurface biosensor for detecting multiple cancers and infectious diseases," *Photonics Nanostruct*, vol. 65, p. 101399, Jul. 2025, doi: 10.1016/J.PHOTONICS.2025.101399.

[23] T. Sheheryar, X. Dong, X. Wang, B. Lv, L. Gao, and B. Xie, "High-Efficiency Graphene-Based Terahertz Polarization Converter with Integrated Biological

Sensing and Tunable Performance," *ACS Applied Optical Materials*, vol. 3, no. 10, pp. 2384–2398, Oct. 2025, doi: 10.1021/ACSAOM.5C00343.

[24] T. Sheheryar, B. Lv, X. Wang, X. Dong, L. Gao, and B. Xie, "Ultra-wideband graphene-assisted Terahertz Sensor with tunable polarization conversion for chemical sensing," *Mater Res Bull*, vol. 195, p. 113806, Mar. 2026, doi: 10.1016/J.MATERRESBULL.2025.113806.

[25] L. Gao, T. Sheheryar, and B. Lv, "Multifunctional terahertz device with angular resilience for biomedical sensing and polarization conversion," *Analyst*, vol. 150, no. 16, pp. 3654–3664, Aug. 2025, doi: 10.1039/D5AN00646E.

[26] T. Sheheryar, B. Lv, and L. Gao, "Dual-functional terahertz metasurface with broadband reflective linear to cross polarization conversion and embedded biosensing," *Optical and Quantum Electronics 2025 57:9*, vol. 57, no. 9, pp. 494-, Aug. 2025, doi: 10.1007/S11082-025-08399-3.

[27] T. Sheheryar, J. Wekalao, B. Lv, and L. Gao, "Ultra-wideband reflecting linear cross polarization converter with integrated high-sensitivity biosensing," *Optical and Quantum Electronics 2025 57:8*, vol. 57, no. 8, pp. 427-, Jul. 2025, doi: 10.1007/S11082-025-08361-3.

[28] H. M. Mamoun, M. F. O. Hameed, O. Hatem, S. T. Assar, S. S. A. Obayya, and M. Y. Azab, "Design of Highly Sensitive Dual-Band THz Metamaterial Sensor for Cancer Early Detection," *Plasmonics*, pp. 1–17, Jul. 2025, doi: 10.1007/S11468-025-03161-7/METRICS.

[29] P. Cao *et al.*, "Tunable Dual-Band Ultrasensitive Stereo Metamaterial Terahertz Sensor," *IEEE Access*, vol. 8, pp. 219525–219533, 2020, doi: 10.1109/ACCESS.2020.3039503.

[30] M. N. Hamza and M. T. Islam, "Designing an Extremely Tiny Dual-Band Biosensor Based on MTMs in the Terahertz Region as a Perfect Absorber for Non-Melanoma Skin Cancer Diagnostics," *IEEE Access*, vol. 11, pp. 136770–136781, 2023, doi: 10.1109/ACCESS.2023.3339562.

[31] X. Lu, H. Ge, Y. Jiang, and Y. Zhang, "A Dual-Band High-Sensitivity THz Metamaterial Sensor Based on Split Metal Stacking Ring," *Biosensors 2022, Vol. 12, Page 471*, vol. 12, no. 7, p. 471, Jun. 2022, doi: 10.3390/BIOS12070471.

[32] A. Teber, "Dual-Band Terahertz Metamaterial Absorber Based on LC Resonance and Dipolar Response and Its Applications," *Adv Theory Simul*, vol. 7, no. 4, p. 2300918, Apr. 2024, doi: 10.1002/ADTS.202300918.

[33] M. Karthikeyan, P. Jayabala, S. Ramachandran, S. S. Dhanabalan, T. Sivanesan, and M. Ponnusamy, "Tunable Optimal Dual Band Metamaterial Absorber for High Sensitivity THz Refractive Index Sensing," *Nanomaterials 2022, Vol. 12, Page 2693*, vol. 12, no. 15, p. 2693, Aug. 2022, doi: 10.3390/NANO12152693.

[34] Y. Zhang *et al.*, "Dual band visible metamaterial absorbers based on four identical ring patches," *Physica E Low Dimens Syst Nanostruct*, vol. 127, p. 114526, Mar. 2021, doi: 10.1016/J.PHYSE.2020.114526.

[35] M. Moniruzzaman *et al.*, "Dual band polarization insensitive metamaterial absorber for EMI shielding from GSM and 5G communication systems," *Sci Rep*, vol. 15, no. 1, pp. 1–18, Dec. 2025, doi: 10.1038/S41598-025-96507-4;SUBJMETA.

[36] D. Wang, K. Da Xu, S. Luo, Y. Cui, L. Zhang, and J. Cui, "A high Q-factor dual-band terahertz metamaterial absorber and its sensing characteristics," *Nanoscale*, vol. 15, no. 7, pp. 3398–3407, Feb. 2023, doi: 10.1039/D2NR05820K.

[37] Z. EL-Wasif, T. Ismail, and O. Hamdy, “Design and optimization of highly sensitive multi-band terahertz metamaterial biosensor for coronaviruses detection,” *Opt Quantum Electron*, vol. 55, no. 7, pp. 1–23, Jul. 2023, doi: https://doi.org/10.1007/s11082-023-04906-6.

[38] R. Mishra, R. Panwar, and D. Singh, “Equivalent circuit model for the design of frequency-selective, terahertz-band, graphene-based metamaterial absorbers,” *IEEE Magn Lett*, vol. 9, pp. 1–5, 2018, doi: 10.1109/LMAG.2018.2878946.

[39] F. Jabbarzadeh, M. Heydari, and A. Habibzadeh-Sharif, “A comparative analysis of the accuracy of Kubo formulations for graphene plasmonics,” *Mater Res Express*, vol. 6, no. 8, p. 086209, May 2019, doi: 10.1088/2053-1591/AB1E02.

[40] A. H. Castro Neto, F. Guinea, N. M. R. Peres, K. S. Novoselov, and A. K. Geim, “The electronic properties of graphene,” *Rev Mod Phys*, vol. 81, no. 1, p. 109, Jan. 2009, doi: 10.1103/RevModPhys.81.109.

[41] G. W. Hanson, “Dyadic green’s functions for an anisotropic, non-local model of biased graphene,” *IEEE Trans Antennas Propag*, vol. 56, no. 3, pp. 747–757, Mar. 2008, doi: 10.1109/TAP.2008.917005.

[42] G. Cerniauskas, H. Sadia, and P. Alam, “Machine intelligence in metamaterials design: a review,” *Oxford Open Materials Science*, vol. 4, no. 1, Jan. 2024, doi: 10.1093/OXFMAT/ITAE001.

[43] S. A. Shampa, M. S. Islam, and A. Nesa, “Machine Learning-based Diabetes Prediction: A Cross-Country Perspective,” *2023 International Conference on Next-Generation Computing, IoT and Machine Learning, NCIM 2023*, 2023, doi: 10.1109/NCIM59001.2023.10212596.

[44] P. Jain *et al.*, “Multiband Metamaterial absorber with absorption prediction by assisted machine learning,” *Mater Chem Phys*, vol. 307, p. 128180, Oct. 2023, doi: 10.1016/J.MATCHEMPHYS.2023.128180.

[45] L. Gu, H. Liu, Z. Wei, R. Wu, and J. Guo, “Optimized Design of Plasma Metamaterial Absorber Based on Machine Learning,” *Photonics 2023, Vol. 10, Page 874*, vol. 10, no. 8, p. 874, Jul. 2023, doi: 10.3390/PHOTONICS10080874.

[46] P. Jain *et al.*, “Machine learning assisted hepta band THz metamaterial absorber for biomedical applications,” *Scientific Reports 2023 13:1*, vol. 13, no. 1, pp. 1–12, Jan. 2023, doi: 10.1038/s41598-023-29024-x.

[47] P. Jain *et al.*, “Machine Learning Techniques for Predicting Metamaterial Microwave Absorption Performance: A Comparison,” *IEEE Access*, vol. 11, pp. 128774–128783, 2023, doi: 10.1109/ACCESS.2023.3332731.